

pubs.acs.org/JACS Communication

# Catalytic Performance and Near-Surface X-ray Characterization of Titanium Hydride Electrodes for the Electrochemical Nitrate Reduction Reaction

Matthew J. Liu, Jinyu Guo, Adam S. Hoffman, Joakim Halldin Stenlid, Michael T. Tang, Elizabeth R. Corson, Kevin H. Stone, Frank Abild-Pedersen, Simon R. Bare, and William A. Tarpeh\*



Cite This: J. Am. Chem. Soc. 2022, 144, 5739-5744



ACCESS I

III Metrics & More



s Supporting Information

**ABSTRACT:** The electrochemical nitrate reduction reaction (NO<sub>3</sub>RR) on titanium introduces significant surface reconstruction and forms titanium hydride (TiH<sub>x</sub>,  $0 < x \le 2$ ). With *ex situ* grazing-incidence X-ray diffraction (GIXRD) and X-ray absorption spectroscopy (XAS), we demonstrated near-surface TiH<sub>2</sub> enrichment with increasing NO<sub>3</sub>RR applied potential and duration. This quantitative relationship facilitated electrochemical treatment of Ti to form TiH<sub>2</sub>/Ti electrodes for use in NO<sub>3</sub>RR, thereby decoupling hydride formation from NO<sub>3</sub>RR performance. A wide range of NO<sub>3</sub>RR activity and selectivity on TiH<sub>2</sub>/Ti electrodes between -0.4 and -1.0 V<sub>RHE</sub> was observed and analyzed with density functional theory (DFT) calculations on TiH<sub>2</sub>(111). This work underscores the importance of relating NO<sub>3</sub>RR performance with near-surface electrode structure to advance catalyst design and operation.

he conversion of wastewater nitrate to ammonia can simultaneously remediate widespread nitrogen pollution and electrify ammonia manufacturing. The electrochemical nitrate reduction reaction (NO<sub>3</sub>RR) has been actively studied because of its potential to circularize nitrogen management. 1-9 As with other electrocatalytic reactions, NO<sub>3</sub>RR electrocatalysts may undergo substantial structural evolution during the reaction, creating a need to understand how the altered catalyst structure influences reaction performance (activity and selectivity). 10-15 Titanium, an inexpensive and abundant metal, has recently been identified as a robust electrocatalytic material for NO<sub>3</sub>RR.<sup>16</sup> The reasons for its catalytic performance remain unclear, especially regarding the role of titanium hydride (TiH<sub>x</sub>,  $0 < x \le 2$ ), a water-stable titanium species that forms during NO<sub>3</sub>RR. The rational operation of Ti-catalyzed NO<sub>3</sub>RR requires improved understanding of how TiH<sub>x</sub> forms and influences NO<sub>3</sub>RR performance.

Metal hydrides have attracted attention for their ability to perform thermal or mechanocatalytic ammonia synthesis from  $N_2$  gas  $^{17-23}$  but remain underexplored for aqueous electrochemical ammonia synthesis (e.g., from nitrate). Electrochemical metal hydride formation proceeds at moderate potentials, acting as a side reaction that convolves electrocatalytic performance with an evolving electrode surface structure. Studies on  $TiH_x$  have demonstrated either quantitative bulk characterization to determine hydrogen content (e.g., X-ray diffraction,  $^{24}$  weight loss,  $^{25}$  outgassing measurements  $^{26}$ ) or qualitative to semiquantitative near-surface (topmost nanometers) characterization (e.g., time-of-flight secondary ion mass spectrometry  $^{27}$ ). Quantitative near-surface characterization has not been reported and is key to overcoming the challenge of decoupling hydride formation from reaction performance. In this work, we combined

systematic synchrotron X-ray characterization of Ti electrodes with electrochemical testing to link near-surface structure (chemical composition, crystal structure, coordination number, and interatomic distance) with NO<sub>3</sub>RR performance. Through ex situ grazing-incidence X-ray diffraction (GIXRD) and total electron yield X-ray absorption spectroscopy (TEY XAS) measurements, we demonstrated the electrochemically tunable enrichment of near-surface TiH<sub>2</sub> by controlling NO<sub>3</sub>RR duration (2 to 8 h) and applied potential (-0.4, -0.6, -0.8, and -1.0  $V_{RHE}$ ). These results informed us about the electrochemical treatment of Ti to produce TiH2/Ti electrodes for use in NO<sub>3</sub>RR. Faradaic efficiency (FE) on TiH<sub>2</sub>/Ti varied greatly with applied potential for the production of ammonia (38.0% to 74.7%) and nitrite (23.9% to 52.3%) but not hydrogen (<2.6%). Meanwhile, partial current density toward ammonia formation on TiH2/Ti increased monotonically with applied potential, reaching -1.83 mA cm<sup>-2</sup> at -1.0 V<sub>RHE</sub>. A surface Pourbaix diagram for the TiH<sub>2</sub>(111) surface was developed from density functional theory (DFT) calculations. Adsorbate free energy diagrams demonstrated that, on  $TiH_2(111)$ , nitrogen species were competitive with H atoms for adsorption in the experimentally studied potential range  $(-0.4 \text{ to } -1.0 \text{ V}_{RHE})$ , which may have contributed to the relatively small amounts of hydrogen evolved. Notably, no appreciable difference in NO<sub>3</sub>RR rate or selectivity was

Received: February 1, 2022 Published: March 22, 2022





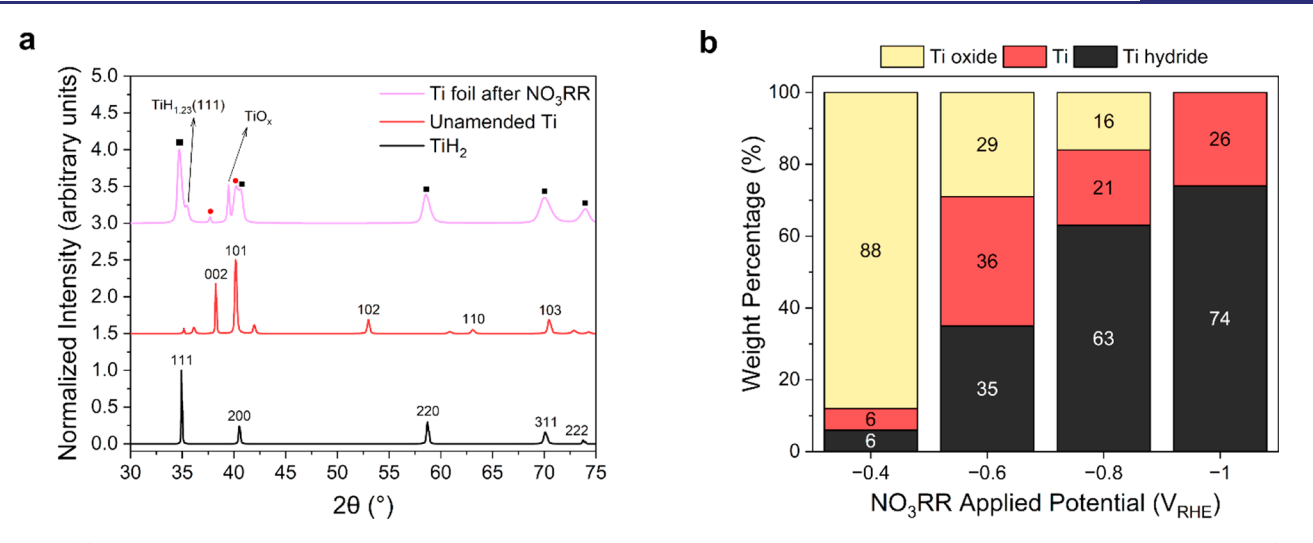


Figure 1. (a) Representative GIXRD of Ti foils before and after electrochemical  $NO_3RR$  ( $-0.6\ V_{RHE}$  for 8 h in 0.1 M  $HClO_4$  + 0.8 mM  $KNO_3$ ) at a nominal probe depth of 3.2 nm. (b) Ti foil chemical compositions calculated from GIXRD after 4 h of  $NO_3RR$  (0.1 M  $HClO_4$  + 0.8 mM  $KNO_3$ ) at varying applied potentials (12.6 nm nominal probe depth).

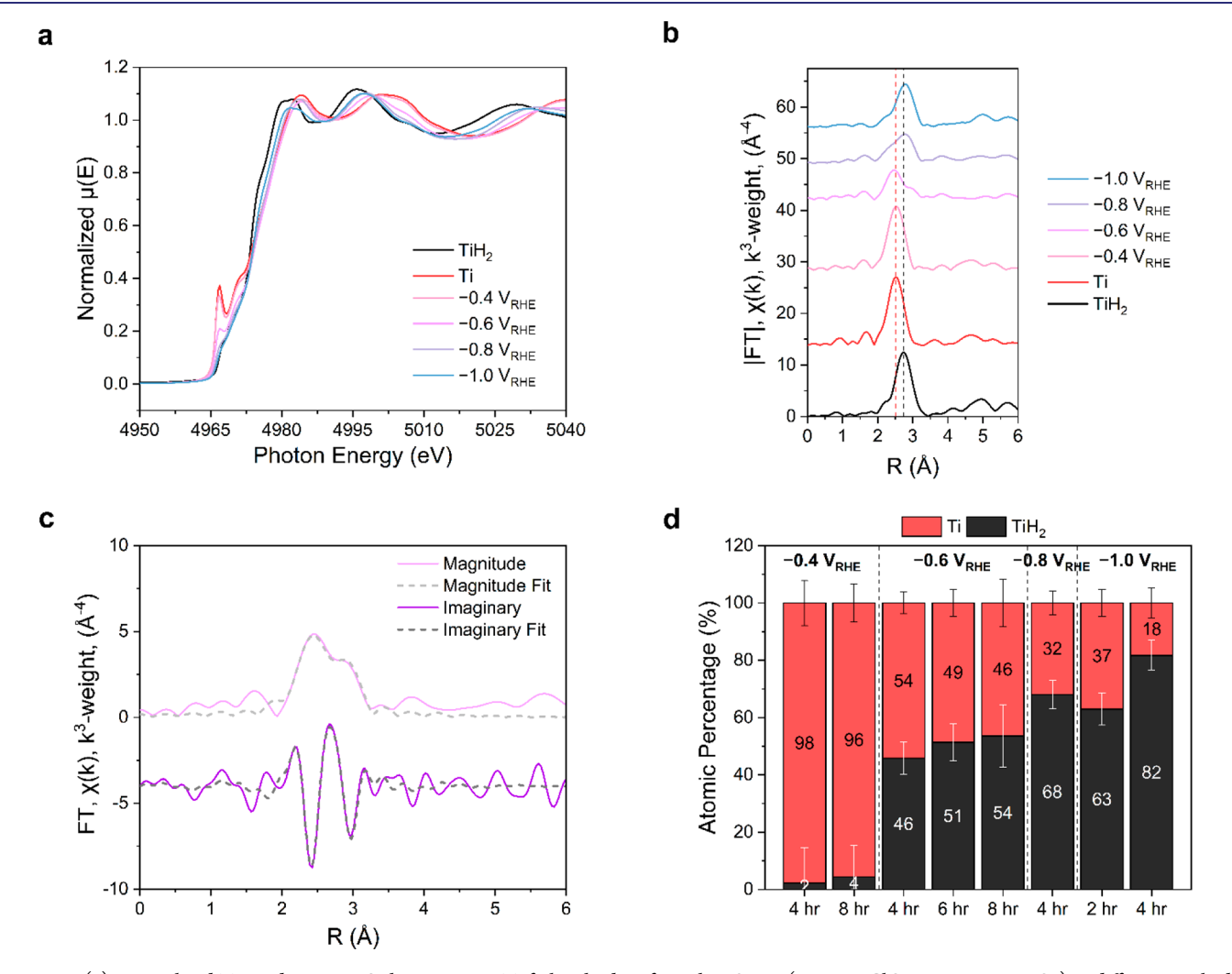
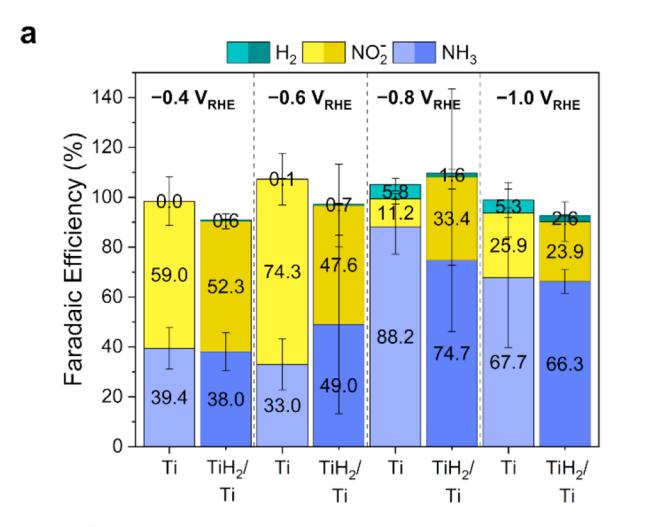


Figure 2. (a) Normalized Ti K-edge XANES characterizing Ti foil cathodes after 4 h NO<sub>3</sub>RR (0.1 M HClO<sub>4</sub> + 0.8 mM KNO<sub>3</sub>) at different applied potentials. (b) Magnitude of the  $k^3$ -weighted Fourier-transformed EXAFS data calculated using a k-range of 3.3–11.6 Å<sup>-1</sup>. Dashed lines correspond to Ti–Ti single-scattering paths for Ti (red) and TiH<sub>2</sub> (black) references. (c)  $k^3$ -weighted Fourier-transformed EXAFS data and best-fit model characterizing the Ti foil cathode after NO<sub>3</sub>RR (-0.6 V<sub>RHE</sub> for 8 h in 0.1 M HClO<sub>4</sub> + 0.8 mM KNO<sub>3</sub>). The k-range and R-range used in the fit were 3.3–11.6 Å<sup>-1</sup> and 1.90–3.25 Å, respectively. (d) Ti atomic percentages obtained from the EXAFS modeling. Error bars represent  $\pm$  one standard deviation scaled by the regression standard error.



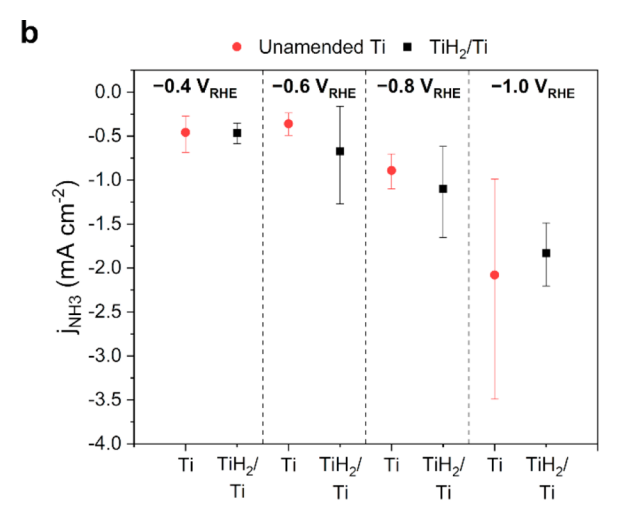


Figure 3. (a) Faradaic efficiencies toward the production of ammonia, nitrite, and hydrogen gas on unamended Ti and  $TiH_2/Ti$  electrodes (1 M NaClO<sub>4</sub> + 10 mM HNO<sub>3</sub> electrolyte). Error bars represent  $\pm$  one standard deviation. (b) Partial current density toward ammonia production on unamended Ti and  $TiH_2/Ti$  electrodes (1 M NaClO<sub>4</sub> + 10 mM HNO<sub>3</sub> electrolyte). Asymmetric error bars come from propagating error (one standard deviation) in total current density and  $FE_{NH3}$ .

observed between unamended Ti (cleaned but not chemically nor electrochemically treated) and  ${\rm TiH_2/Ti}$  electrodes, suggesting that both the rate-determining and selectivity-determining steps were negligibly affected by the initial near-surface structure of the electrodes.

With GIXRD, we characterized the crystalline structure of commercially pure, polycrystalline Ti foil cathodes before and after NO<sub>3</sub>RR (experimental matrix in Table S3).  $\alpha$ -Ti was the major phase in the diffractograms of unamended Ti foil. Over the course of NO<sub>3</sub>RR, the Ti electrodes shared significant and consistent structural alterations across the applied potentials, durations, and nominal probe depths tested (chemical composition estimates from each diffractogram in Figures S4–S15). The  $\alpha$ -Ti diffraction peaks decreased in relative peak area, often becoming the nondominant phase (Figure 1a). Meanwhile, diffraction patterns for TiH<sub>x</sub> appeared, the most intense of which came from TiH<sub>2</sub> and the less intense of which corresponded to crystalline, substoichiometric TiH<sub>v</sub>. Altogether,  $\alpha$ -Ti, TiO<sub>x</sub> (0 < x  $\leq$  2), and TiH<sub>x</sub> coexisted in post-NO<sub>3</sub>RR electrodes, and no other crystalline titanium species (e.g., titanium nitride) were observed. For a fixed NO<sub>3</sub>RR duration and nominal probe depth, a more negative applied potential led to enriched hydride content (Figure 1b). Likewise, longer NO<sub>3</sub>RR durations led to enriched hydride content though to a lesser extent than the applied potential.

To complement GIXRD, Ti K-edge TEY XAS measurements (nominal probe depth of  $5-10~\rm nm^{28-31}$ ) were used to sample the ensemble average of local Ti coordination environments at the electrode near-surface. The X-ray absorption near-edge structure (XANES, Figure 2a) of unamended Ti showed a characteristic pre-edge peak corresponding to a Ti 1s  $\rightarrow$  3d transition. The peak was absent in TiH<sub>2</sub>, indicating its cubic (fcc) structure and facilitating TiH<sub>2</sub> assignment in samples of various applied potentials and durations. Ti foil from 4 h of NO<sub>3</sub>RR at -0.4 and  $-0.6~\rm V_{RHE}$  showed a pre-edge peak similar to that of the Ti foil but diminished in intensity, while analogous samples from NO<sub>3</sub>RR at  $-0.8~\rm and$   $-1.0~\rm V_{RHE}$  showed no pre-edge peak, suggesting a near-surface structure transition from  $\alpha$ -Ti (hcp) to TiH<sub>2</sub> (fcc). In the Fourier transform of the extended X-ray absorption fine structure (EXAFS), a pronounced peak

corresponding to Ti-Ti scattering occurred at 2.52 Å for Ti foil and -0.4 and -0.6 V<sub>RHE</sub> NO<sub>3</sub>RR samples (Figure 2b). This peak was shifted to 2.79 Å for  $TiH_2$  and -0.8 and -1.0V<sub>RHE</sub> NO<sub>3</sub>RR samples, corresponding to a 10.7% expansion. EXAFS modeling was performed with bonding distance Ti-Ti scattering paths from both Ti and TiH2 (representative fits in Figure 2c). The resulting coordination numbers from each sample are given in Table S1 and shown as atomic percentages in Figure 2d. XANES, k³-weighted EXAFS, Fourier-transformed EXAFS, and EXAFS fits for the complete set of samples are presented in Figures S24-S36. The number of Ti atoms belonging to TiH2 consistently increased with both applied potential and duration, while Ti belonging to  $\alpha$ -Ti exhibited the opposite trend. In agreement with GIXRD, a more negative applied potential enriched near-surface hydride content more drastically than longer applied durations. For example, more TiH<sub>2</sub> was formed at  $-1.0 \text{ V}_{\text{RHE}}$  (2 h) than -0.6V<sub>RHE</sub> (8 h). The evident control over the near-surface structure enabled electrochemical treatment of Ti to produce TiH<sub>2</sub>/Ti electrodes (Section S3.2 and Figure S37) for use in NO<sub>3</sub>RR.

The electrochemical NO<sub>3</sub>RR performance of unamended Ti and preformed TiH<sub>2</sub>/Ti electrodes was assessed with 30-min chronoamperometry experiments at -0.4, -0.6, -0.8, and  $-1.0 \text{ V}_{\text{RHE}}$  (1 M NaClO<sub>4</sub> + 10 mM HNO<sub>3</sub>, Section S3.2). GIXRD of unamended Ti electrodes after chronoamperometry showed no TiHx phase, while the persistence of near-surface TiH<sub>2</sub> was observed on TiH<sub>2</sub>/Ti electrodes (Figures S16–S23). Faradaic efficiency toward  $H_2$  (FE<sub>H2</sub>) remained below 5.8  $\pm$ 2.5% (Figure 3a), indicating that NO<sub>3</sub>RR was the dominant reaction and that TiH<sub>2</sub>/Ti electrodes did not introduce appreciable HER competition. Nitrite was the major reaction product at -0.4 and -0.6  $V_{\text{RHE}}$  while ammonia dominated at -0.8 and −1.0 V<sub>RHE</sub>; negligible N<sub>2</sub> production was observed (50 ppm detection limit). FE<sub>NH3</sub> ratios of TiH<sub>2</sub>/Ti to unamended Ti showed no significant difference between the applied potentials investigated (Figure S38). The ratios of NH<sub>3</sub> N-selectivity (fraction of reacted nitrate converted to ammonia) followed a similar trend (Figure S39), suggesting that the selectivity-determining step of NO<sub>3</sub>RR remained unchanged between unamended Ti and TiH2/Ti electrodes. An analogous conclusion was reached by examining the

performance metrics for electrocatalytic activity ( $j_{\rm NH3}$  in Figure 3b and nitrate conversion in Figure S40). Several reasons may explain the similar NO<sub>3</sub>RR performance. Although both electrodes began with different near-surface structures, in situ catalytic conditions may have led to a convergence of surface structure and therefore similar reactivity. Alternatively, the electrode surfaces may have remained distinct, yet other factors played a more dominating role in conferring reaction performance, such as surface roughness or contributions to surface electronic state imparted by the coexistence of Ti,  ${\rm TiO}_{x'}$  and  ${\rm TiH}_{x'}$ .

To provide insights into the reactivity of TiH2, periodic DFT calculations on the thermodynamics of surface coverage were performed using the RPBE xc-functional in the Vienna Ab-initio Simulation Package (Section S4).34-36 A surface Pourbaix diagram (Figure 4a, surface and adsorption structures in Figure 4c) was developed for TiH<sub>2</sub>(111), the most intense TiH<sub>2</sub> peak observed via GIXRD, to summarize H\* coverage  $(\theta_{\rm H})$  under standard conditions. For TiH<sub>2</sub>,  $\theta_{\rm H}$  is defined as the coverage of hydrogen following a full monolayer in all available hcp sites. The hydrogen evolution reaction (HER) is thermodynamically favorable over H\* adsorption once the hcp sites become occupied, and if HER is kinetically available, this will lead to a lowering of  $\theta_{\rm H}$ . From thermodynamics,  $\theta_{\rm H}$ increases with more negative applied potentials up to a TiH2terminated surface. For a fixed applied potential,  $\theta_{\mathrm{H}}$  may sharply decrease with increasing pH, which we indeed observed in the catholyte for all electrochemical experiments (as drastic as pH 1.70 to 11.85, Figure S41). We therefore hypothesize that transient  $\theta_{\mathrm{H}}$  plays a role in steering the reaction selectivities seen in Figure 3a, such as by controlling hydrogenation of surface intermediates to form NO<sub>x</sub>\* and NH<sub>v</sub>\* species.<sup>37,38</sup> Our calculated potential of zero charge (negative of  $-1.0 \text{ V}_{\text{RHE}}$  for nearly all  $\theta_{\text{H}}$ , Table S5) leads to a positively charged surface, likely promoting anionic nitrate adsorption, which is often the rate-determining step of NO<sub>3</sub>RR.<sup>7,39</sup> The DFT calculations predict that, regardless of the initial  $\theta_{\rm H}$ , nitrogen species are competitive for surface sites compared to H (Figure 4b). While molecular nitrate (NO<sub>3</sub>\*) exhibits weak adsorption that gets weaker with increasing NO<sub>3</sub>RR overpotential, dissociative adsorption into nitrite  $(NO_2^*)$  and surface (hydr)oxide,  $O(H)^*$ , is favorable. The stability of coadsorbed O\* and OH\* relative to the oxidized  $H_2O_{(aq)}$  state varies significantly with potential (Figures 4b and S43 for high coverage), and understanding the competition between nitrogen and oxygen surface species may elucidate the potential dependence of NO<sub>3</sub>RR products over TiH<sub>2</sub>. Lastly, preliminary DFT calculations on Ti(0001) indicate that the integral free energies of H\* under one monolayer are lower than the integral free energy to evolve H<sub>2</sub> (Figure S44), implying that unamended Ti will eventually form surface TiH<sub>2</sub> under NO<sub>3</sub>RR conditions. The analysis suggests that similar reactivity to TiH2/Ti electrodes may be conferred to unamended Ti in situ; this in situ modification may be more influential than ex situ pretreatment.

In summary, electrochemical preparation and testing of TiH<sub>2</sub>/Ti electrodes was enabled by systematically characterizing the Ti near-surface. Electrochemical experiments paired with DFT calculations indicate that the applied potentials explored in this work correspond to a fundamentally dynamic range of NO<sub>3</sub>RR activity and selectivity on TiH<sub>2</sub>. Our investigation advances direct relationships between NO<sub>3</sub>RR performance with *ex situ* near-surface electrocatalyst compo-

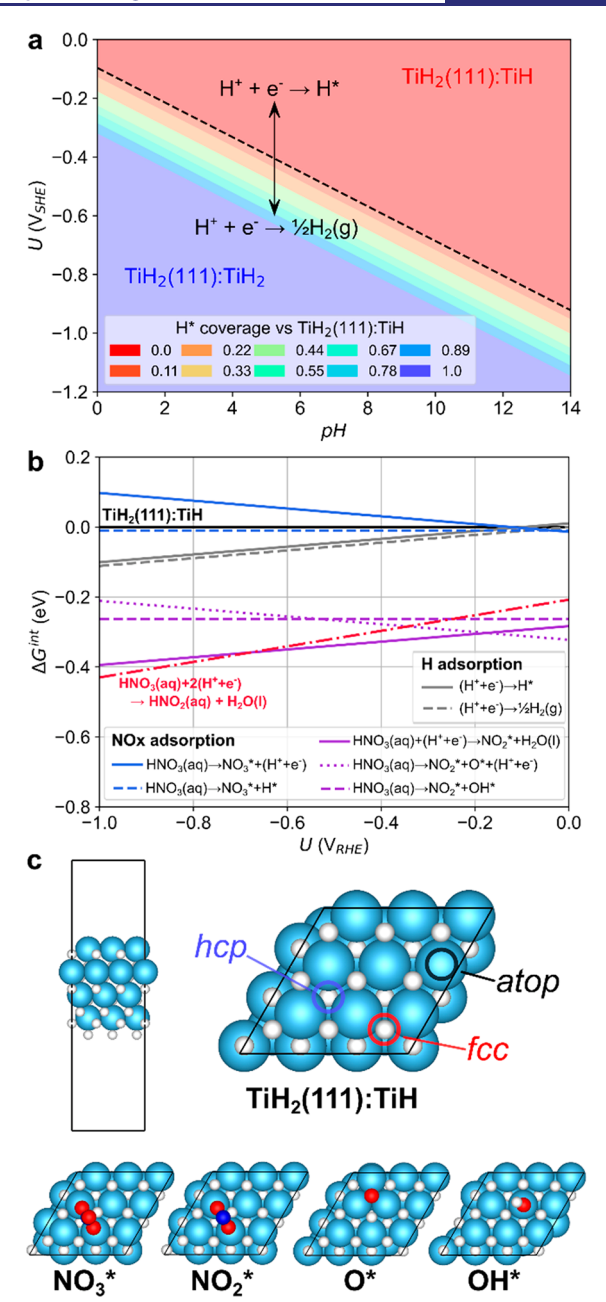


Figure 4. (a) Surface Pourbaix diagram for the  $TiH_2(111)$  surface with TiH termination (Section S4.2 and Figure S42), denoted as  $TiH_2(111)$ :TiH. Color scale indicates prevalent surface  $H^*$  (hcp site) coverage evaluated on a 3  $\times$  3 unit cell. The black dotted line indicates where  $H_2(g)$  formation is thermodynamically favored over  $H^*$  adsorption. (b) Integral free energy (normalized by number of sites),  $\Delta G^{\rm int}$ , at the standard state of  $NO_3RR$  intermediates for low coverage on  $TiH_2(111)$ :TiH. (c)  $TiH_2(111)$ :TiH surface and optimized adsorption structures of  $NO_3RR$  intermediates. Adsorption sites on the surface are depicted with additional  $H^*$ , preferring the hcp hollow site by 0.58 eV/H over the atop site occupied in epitaxial growth.  $NO_3^*$  and  $NO_2^*$  adsorb in bidentate mode on the atop sites;  $O^*$  sits in the hcp site, and  $OH^*$  sits on the atop site.

sition and identifies key opportunities for further research, such as kinetic DFT calculations and *in situ* characterization of Ti electrodes.

### ASSOCIATED CONTENT

# **3** Supporting Information

The Supporting Information is available free of charge at https://pubs.acs.org/doi/10.1021/jacs.2c01274.

Experimental details; supporting tables; data processing and fitting; DFT methodology; additional GIXRD, XAS, and electrochemical data (PDF)

### AUTHOR INFORMATION

## **Corresponding Author**

William A. Tarpeh – Department of Chemical Engineering, Stanford University, Stanford, California 94305, United States; SUNCAT Center for Interface Science and Catalysis, SLAC National Accelerator Laboratory, Menlo Park, California 94025, United States; ◎ orcid.org/0000-0002-2950-526X; Email: wtarpeh@stanford.edu

### **Authors**

Matthew J. Liu − Department of Chemical Engineering, Stanford University, Stanford, California 94305, United States; ② orcid.org/0000-0002-8496-8267

Jinyu Guo — Department of Chemical Engineering, Stanford University, Stanford, California 94305, United States;
orcid.org/0000-0002-8775-3085

Adam S. Hoffman – Stanford Synchrotron Radiation Lightsource, SLAC National Accelerator Laboratory, Menlo Park, California 94025, United States; orcid.org/0000-0002-7682-4108

Joakim Halldin Stenlid — Department of Chemical Engineering, Stanford University, Stanford, California 94305, United States; SUNCAT Center for Interface Science and Catalysis, SLAC National Accelerator Laboratory, Menlo Park, California 94025, United States; orcid.org/0000-0003-3832-2331

Michael T. Tang — Department of Chemical Engineering, Stanford University, Stanford, California 94305, United States; SUNCAT Center for Interface Science and Catalysis, SLAC National Accelerator Laboratory, Menlo Park, California 94025, United States; orcid.org/0000-0002-7190-4723

Elizabeth R. Corson — Department of Chemical Engineering, Stanford University, Stanford, California 94305, United States; © orcid.org/0000-0003-2722-674X

Kevin H. Stone — Stanford Synchrotron Radiation Lightsource, SLAC National Accelerator Laboratory, Menlo Park, California 94025, United States; ocid.org/0000-0003-1387-1510

Frank Abild-Pedersen — SUNCAT Center for Interface Science and Catalysis, SLAC National Accelerator Laboratory, Menlo Park, California 94025, United States; orcid.org/0000-0002-1911-074X

Simon R. Bare — Stanford Synchrotron Radiation Lightsource, SLAC National Accelerator Laboratory, Menlo Park, California 94025, United States; SUNCAT Center for Interface Science and Catalysis, SLAC National Accelerator Laboratory, Menlo Park, California 94025, United States; orcid.org/0000-0002-4932-0342

Complete contact information is available at: https://pubs.acs.org/10.1021/jacs.2c01274

# **Author Contributions**

\*M.J.L. and J.G. contributed equally to this work.

### Notes

The authors declare no competing financial interest.

### ACKNOWLEDGMENTS

We are grateful to several funders of this work, including the National Science Foundation EFRI program (Award 2132007) and the Chemical Engineering Department at Stanford University. M.J.L. acknowledges support from the National Aeronautics and Space Administration (NASA) Space Technology Graduate Research Opportunities fellowship (Award 80NSSC20K1207). J.G. and E.R.C. acknowledge support from the TomKat Center for Sustainable Energy. Co-ACCESS is supported by the U.S. Department of Energy, Office of Basic Energy Sciences, Chemical Sciences, Geosciences and Biosciences Division. J.H.S., M.T.T., F.A-P., and S.R.B. acknowledge support from the U.S. Department of Energy, Office of Science, Office of Basic Energy Sciences, Chemical Sciences, Geosciences, and Biosciences Division, Catalysis Science Program to the SUNCAT Center for Interface Science and Catalysis. J.H.S. acknowledges support from the Knut and Alice Wallenberg Foundation (grant no. 2019.0586). We acknowledge computational support from the National Energy Research Scientific Computing Center (Project Allocation No. m2997), a Department of Energy Office of Science User Facility supported by the Office of Science of the U.S. Department of Energy under Contract No. DE-AC02-05CH11231. Part of this work was performed at beamline 2-1 at the Stanford Synchrotron Radiation Lightsource, SLAC National Accelerator Laboratory, which is supported by the U.S. Department of Energy, Office of Science, Office of Basic Energy Sciences under Contract No. DE-AC02-76SF00515. Part of this work was performed at the Stanford Nano Shared Facilities (SNSF), supported by the National Science Foundation under award ECCS-2026822. The authors thank José A. Zamora Zeledón for insights on GIXRD data processing; Laura Mundt, Anthony Y. Fong, and Arturas Vailionis for assistance collecting diffractograms; Boon Siong Neo for statistical interpretation of EXAFS modeling results; the Tarpeh lab for critical feedback on the research project; Carolina Muñoz for fruitful discussions, support, and inspiration.

# REFERENCES

- (1) Katsounaros, I. On the Assessment of Electrocatalysts for Nitrate Reduction. *Current Opinion in Electrochemistry* **2021**, *28*, 100721.
- (2) van Langevelde, P. H.; Katsounaros, I.; Koper, M. T. M. Electrocatalytic Nitrate Reduction for Sustainable Ammonia Production. *Joule* **2021**, *5* (2), 290–294.
- (3) Chen, G.-F.; Yuan, Y.; Jiang, H.; Ren, S.-Y.; Ding, L.-X.; Ma, L.; Wu, T.; Lu, J.; Wang, H. Electrochemical Reduction of Nitrate to Ammonia via Direct Eight-Electron Transfer Using a Copper-Molecular Solid Catalyst. *Nat. Energy* **2020**, *5* (8), 605–613.
- (4) Wu, Z.-Y.; Karamad, M.; Yong, X.; Huang, Q.; Cullen, D. A.; Zhu, P.; Xia, C.; Xiao, Q.; Shakouri, M.; Chen, F.-Y.; Kim, J. Y.; Xia, Y.; Heck, K.; Hu, Y.; Wong, M. S.; Li, Q.; Gates, I.; Siahrostami, S.; Wang, H. Electrochemical Ammonia Synthesis via Nitrate Reduction on Fe Single Atom Catalyst. *Nat. Commun.* **2021**, *12* (1), 2870.
- (5) Li, P.; Jin, Z.; Fang, Z.; Yu, G. A Single-Site Iron Catalyst with Preoccupied Active Centers That Achieves Selective Ammonia Electrosynthesis from Nitrate. *Energy Environ. Sci.* **2021**, *14* (6), 3522–3531.
- (6) Zeng, Y.; Priest, C.; Wang, G.; Wu, G. Restoring the Nitrogen Cycle by Electrochemical Reduction of Nitrate: Progress and Prospects. *Small Methods* **2020**, *4* (12), 2000672.

- (7) Garcia-Segura, S.; Lanzarini-Lopes, M.; Hristovski, K.; Westerhoff, P. Electrocatalytic Reduction of Nitrate: Fundamentals to Full-Scale Water Treatment Applications. *Applied Catalysis B: Environmental* **2018**, 236, 546–568.
- (8) Rosca, V.; Duca, M.; de Groot, M. T.; Koper, M. T. M. Nitrogen Cycle Electrocatalysis. *Chem. Rev.* **2009**, *109* (6), 2209–2244.
- (9) Martínez, J.; Ortiz, A.; Ortiz, I. State-of-the-Art and Perspectives of the Catalytic and Electrocatalytic Reduction of Aqueous Nitrates. *Applied Catalysis B: Environmental* **2017**, 207, 42–59.
- (10) Hahn, C.; Hatsukade, T.; Kim, Y.-G.; Vailionis, A.; Baricuatro, J. H.; Higgins, D. C.; Nitopi, S. A.; Soriaga, M. P.; Jaramillo, T. F. Engineering Cu Surfaces for the Electrocatalytic Conversion of CO<sub>2</sub>: Controlling Selectivity toward Oxygenates and Hydrocarbons. *Proc. Natl. Acad. Sci. U. S. A.* **2017**, 114 (23), 5918–5923.
- (11) Tan, X.; Yu, C.; Zhao, C.; Huang, H.; Yao, X.; Han, X.; Guo, W.; Cui, S.; Huang, H.; Qiu, J. Restructuring of Cu<sub>2</sub>O to Cu<sub>2</sub> O@Cu-Metal-Organic Frameworks for Selective Electrochemical Reduction of CO<sub>2</sub>. ACS Appl. Mater. Interfaces **2019**, 11 (10), 9904–9910.
- (12) Karapinar, D.; Huan, N. T.; Ranjbar Sahraie, N.; Li, J.; Wakerley, D.; Touati, N.; Zanna, S.; Taverna, D.; Galvão Tizei, L. H.; Zitolo, A.; Jaouen, F.; Mougel, V.; Fontecave, M. Electroreduction of CO<sub>2</sub> on Single-Site Copper-Nitrogen-Doped Carbon Material: Selective Formation of Ethanol and Reversible Restructuration of the Metal Sites. *Angew. Chem., Int. Ed.* **2019**, *58* (42), 15098–15103.
- (13) Deng, B.; Huang, M.; Li, K.; Zhao, X.; Geng, Q.; Chen, S.; Xie, H.; Dong, X.; Wang, H.; Dong, F. The Crystal Plane Is Not the Key Factor for CO<sub>2</sub>-to-Methane Electrosynthesis on Reconstructed Cu<sub>2</sub>O Microparticles. *Angew. Chem., Int. Ed.* **2022**, *61* (7), e202114080.
- (14) Motahar Hossain, Md.; Nakata, K.; Kawaguchi, T.; Shimazu, K. Reduction of Nitrate on Electrochemically Pre-Reduced Tin-Modified Palladium Electrodes. *J. Electroanal. Chem.* **2013**, 707, 59–65.
- (15) Fu, W.; Hu, Z.; Zheng, Y.; Su, P.; Zhang, Q.; Jiao, Y.; Zhou, M. Tuning Mobility of Intermediate and Electron Transfer to Enhance Electrochemical Reduction of Nitrate to Ammonia on Cu<sub>2</sub>O/Cu Interface. *Chemical Engineering Journal* **2022**, 433, 133680.
- (16) McEnaney, J. M.; Blair, S. J.; Nielander, A. C.; Schwalbe, J. A.; Koshy, D. M.; Cargnello, M.; Jaramillo, T. F. Electrolyte Engineering for Efficient Electrochemical Nitrate Reduction to Ammonia on a Titanium Electrode. ACS Sustainable Chem. Eng. 2020, 8 (7), 2672–2681
- (17) Kobayashi, Y.; Tang, Y.; Kageyama, T.; Yamashita, H.; Masuda, N.; Hosokawa, S.; Kageyama, H. Titanium-Based Hydrides as Heterogeneous Catalysts for Ammonia Synthesis. *J. Am. Chem. Soc.* **2017**, *139* (50), 18240–18246.
- (18) Tsuji, Y.; Okazawa, K.; Kobayashi, Y.; Kageyama, H.; Yoshizawa, K. Electronic Origin of Catalytic Activity of  $TiH_2$  for Ammonia Synthesis. *J. Phys. Chem. C* **2021**, *125* (7), 3948–3960.
- (19) Han, G.-F.; Li, F.; Chen, Z.-W.; Coppex, C.; Kim, S.-J.; Noh, H.-J.; Fu, Z.; Lu, Y.; Singh, C. V.; Siahrostami, S.; Jiang, Q.; Baek, J.-B. Mechanochemistry for Ammonia Synthesis under Mild Conditions. *Nat. Nanotechnol.* **2021**, *16* (3), 325–330.
- (20) Tricker, A. W.; Hebisch, K. L.; Buchmann, M.; Liu, Y.-H.; Rose, M.; Stavitski, E.; Medford, A. J.; Hatzell, M. C.; Sievers, C. Mechanocatalytic Ammonia Synthesis over TiN in Transient Microenvironments. ACS Energy Lett. 2020, 5 (11), 3362–3367.
- (21) Tang, Y.; Kobayashi, Y.; Masuda, N.; Uchida, Y.; Okamoto, H.; Kageyama, T.; Hosokawa, S.; Loyer, F.; Mitsuhara, K.; Yamanaka, K.; Tamenori, Y.; Tassel, C.; Yamamoto, T.; Tanaka, T.; Kageyama, H. Metal-Dependent Support Effects of Oxyhydride-Supported Ru, Fe, Co Catalysts for Ammonia Synthesis. *Adv. Energy Mater.* **2018**, 8 (36), 1801772.
- (22) Cao, Y.; Saito, A.; Kobayashi, Y.; Ubukata, H.; Tang, Y.; Kageyama, H. Vanadium Hydride as an Ammonia Synthesis Catalyst. *ChemCatChem.* **2021**, *13* (1), 191–195.
- (23) Wang, Q.; Pan, J.; Guo, J.; Hansen, H. A.; Xie, H.; Jiang, L.; Hua, L.; Li, H.; Guan, Y.; Wang, P.; Gao, W.; Liu, L.; Cao, H.; Xiong, Z.; Vegge, T.; Chen, P. Ternary Ruthenium Complex Hydrides for Ammonia Synthesis via the Associative Mechanism. *Nat. Catal* **2021**, *4* (11), 959–967.

- (24) Millenbach, P.; Givon, M. The Electrochemical Formation of Titanium Hydride. *Journal of the Less Common Metals* **1982**, 87 (2), 179–184.
- (25) Videm, K.; Lamolle, S.; Monjo, M.; Ellingsen, J. E.; Lyngstadaas, S. P.; Haugen, H. J. Hydride Formation on Titanium Surfaces by Cathodic Polarization. *Appl. Surf. Sci.* **2008**, 255 (5), 3011–3015.
- (26) Rodrigues, D. C.; Urban, R. M.; Jacobs, J. J.; Gilbert, J. L. In Vivo Severe Corrosion and Hydrogen Embrittlement of Retrieved Modular Body Titanium Alloy Hip-Implants. *J. Biomed Mater. Res. B Appl. Biomater* **2009**, 88B (1), 206–219.
- (27) Liu, Y.; Ren, Z. H.; Liu, J.; Schaller, R. F.; Asselin, E. Electrochemical Investigation and Identification of Titanium Hydrides Formed in Mixed Chloride Sulfuric Acid Solution. *J. Electrochem. Soc.* **2019**, *166* (11), C3096–C3105.
- (28) Hähner, G. Near Edge X-Ray Absorption Fine Structure Spectroscopy as a Tool to Probe Electronic and Structural Properties of Thin Organic Films and Liquids. *Chem. Soc. Rev.* **2006**, *35* (12), 1244–1255.
- (29) Gao, X.; Xu, H.; Wee, A. T. S.; Kuch, W.; Tieg, C.; Wang, S. Magnetic Circular Dichroism Study of Fe/Co/Cu(001) Using Electron Yield X-Ray Absorption Spectroscopy with Different Probe Depths. J. Appl. Phys. 2005, 97 (10), 103527.
- (30) Lee, J.-S.; Xie, Y. W.; Sato, H. K.; Bell, C.; Hikita, Y.; Hwang, H. Y.; Kao, C.-C. Titanium Dx y Ferromagnetism at the LaAlO<sub>3</sub>/SrTiO<sub>3</sub> Interface. *Nat. Mater.* **2013**, *12* (8), 703–706.
- (31) Filatova, E. O.; Konashuk, A. S.; Sakhonenkov, S. S.; Sokolov, A. A.; Afanas'ev, V. V. Re-Distribution of Oxygen at the Interface between  $\gamma$ -Al<sub>2</sub>O<sub>3</sub> and TiN. *Sci. Rep* **2017**, 7 (1), 4541.
- (32) DeBeer George, S.; Huang, K.-W.; Waymouth, R. M.; Solomon, E. I. Metal and Ligand K-Edge XAS of Titanium-TEMPO Complexes: Determination of Oxidation States and Insights into Ti-O Bond Homolysis. *Inorg. Chem.* **2006**, *45* (11), 4468–4477.
- (33) Magnuson, M.; Eriksson, F.; Hultman, L.; Högberg, H. Bonding Structures of ZrH<sub>x</sub> Thin Films by X-Ray Spectroscopy. *J. Phys. Chem. C* **2017**, *121* (46), 25750–25758.
- (34) Hammer, B.; Hansen, L. B.; Nørskov, J. K. Improved Adsorption Energetics within Density-Functional Theory Using Revised Perdew-Burke-Ernzerhof Functionals. *Phys. Rev. B* **1999**, 59 (11), 7413–7421.
- (35) Kresse, G.; Hafner, J. Ab Initio Molecular Dynamics for Liquid Metals. Phys. Rev. B 1993, 47 (1), 558-561.
- (36) Kresse, G.; Furthmüller, J. Efficient Iterative Schemes for *Ab Initio* Total-Energy Calculations Using a Plane-Wave Basis Set. *Phys. Rev. B* **1996**, *54* (16), 11169–11186.
- (37) Song, H.; Tan, Y. C.; Kim, B.; Ringe, S.; Oh, J. Tunable Product Selectivity in Electrochemical  $\rm CO_2$  Reduction on Well-Mixed Ni-Cu Alloys. *ACS Appl. Mater. Interfaces* **2021**, 13 (46), 55272–55280.
- (38) Liu, J.-X.; Richards, D.; Singh, N.; Goldsmith, B. R. Activity and Selectivity Trends in Electrocatalytic Nitrate Reduction on Transition Metals. *ACS Catal.* **2019**, *9* (8), 7052–7064.
- (39) Duca, M.; Koper, M. T. M. Powering Denitrification: The Perspectives of Electrocatalytic Nitrate Reduction. *Energy Environ. Sci.* **2012**, *5* (12), 9726–9742.